Numerical experiments on granulation-generated two-fluid waves and flows in a solar magnetic carpet

R. Niedziela,[1] K. Murawski,[1] A.K. Srivastava[2]
[1]*Institute of Physics, University of M. Curie-Skłodowska, Pl. M. Curie-Skłodowskiej 1, 20-031 Lublin, Poland*
[2]*Department of Physic, Indian Institute of Technology (BHU), Varanasi-221005, India*

4 October 2024

ABSTRACT

We consider the effects of granulation with a complex geometry of a magnetic carpet on the genesis of waves and plasma flows in a quiet-region of the solar atmosphere. Our aim is to perform numerical experiments on the self-generated and self-evolving solar granulation in a magnetic carpet representing the parts of the large-scale magnetized solar atmosphere, where waves and flows are basic inherent physical processes occurring continuously. We perform numerical experiments with the use of the JOANNA code which solves non-ideal and non-adiabatic two-fluid equations for ions+electrons and neutrals treated as two separate fluids. In these experiments, we assume that the plasma is hydrogen, and initially described by magnetohydrostatic equilibrium which is accompanied with a magnetic carpet. Parametric studies with different values of magnetic field show that its higher values result in larger magnitudes of ion-neutral velocity drift, thus ensuring larger heating and plasma flows. The present model addresses that in the highly dynamic solar chromosphere, waves, heating and plasma flows may collectively couple different layers of the solar atmosphere, and this entire process crucially depends on the local plasma and magnetic field properties. We suggest that waves and flows are the natural response of the granulation process in the quiet-Sun.

Key words: Sun: atmosphere – Sun: granulation – methods: numerical

1 INTRODUCTION

It is well established that the plasma and radiative properties of the solar atmosphere change with altitude leading to an increase in its temperature and thus in the ionization level of the species present in its higher layers (Avrett & Loeser 2008). However, the bottom layer of the Sun's atmosphere, called the photosphere, is characterized by a temperature range from about 5600 K at its bottom to about 4300 K at its top. Such low temperature leads to a weakly ionized plasma (Khomenko et al. 2014). Investigation of the small-scale magnetic activity of the three-dimensional (3D) quiet solar atmosphere models reveals mean field strength $\langle B \rangle \approx 70$ G in the middle of the photosphere (del Pino Alemán et al. 2018). The photosphere is capped by the chromosphere, where temperature rises to almost 7×10^3 K. The ionization level, therefore, subsequently increases and the plasma becomes partially ionized. The temperature in the outermost layer, known as the solar corona, reaches to $1 - 3$ MK, and the plasma becomes fully ionized there. The high-degree of rise in the temperature in upper layers of the solar atmosphere remains an unsolved problem, and consists of several components related to wave heating and magnetic field interactions (e.g., Srivastava et al. 2021; Li et al. 2024). Such complex plasma requires a special treatment. One of the models, which can be used to describe weakly and partially ionized plasma, is based on the two-fluid equations (e.g. Zaqarashvili et al. 2011). This model naturally takes into account ion-neutral collisions (Ballester et al. 2018) which result in wave damping and consequently in wave energy thermalization (Forteza et al. 2007; Erdélyi & James 2004). The last studies of the two-fluid waves performed by Niedziela et al. (2022), Murawski et al. (2022) and Pelekhata et al. (2023) show their contribution to chromosphere heating and generation of plasma outflows in the low corona.

It is likely that convective movements of plasma under the solar surface lead to the formation of solar granulation, and they can be a source of many dynamical events and excitation of waves (e.g. Vigeesh et al. 2017).

In this context, convective cells and magnetic field, together form magneto-convection (Proctor 2004). The generation and propagation of magnetoacoustic waves due to granulation was widely studied (e.g. Hansteen et al. 2006; Heggland et al. 2011). Additionally, Martínez-Sykora et al. (2017) investigated excitation of solar spicules and Alfvén waves in the 2.5-dimensional (2.5D) model with solar granulation. Recent studies of the two-fluid waves generated by spontaneously generated and self-evolving convection show that a wide spectrum of wave periods is generated by the granulation (Wójcik et al. 2020). In the later studies, Fleck et al. (2021) performed numerical simulations of acoustic-gravity waves generated by the solar granulation and confirmed that only short-period acoustic and long-period gravity waves are able to reach the corona.

Along similar lines, Murawski et al. (2022) studied chromosphere heating and generation of plasma outflows associated with two-fluid solar granulation. However, initially (at $t = 0$ s) straight vertical magnetic field was considered. The major aim of this paper is to extend the model of Murawski et al. (2022) by supplementing the vertical magnetic field by a more realistic solar magnetic carpet which naturally occupies the solar atmosphere in the form of magnetic arcades (Parnell 2002). Such magnetic carpet is expected to significantly affect the dynamics of the localized solar atmosphere and, as

a result, influences chromosphere heating and plasma flows inherent therein.

In the present paper, we illustrate the comperehensive physical scenario of the self-consistent evolution of waves and flows excited by the granulation, operating in the two regimes of magnetic carpet. We also emphasize on the dependence of these physical processes on the intensity of the magnetic field.

This paper is organized as follows. In the following section, the numerical model is described. Section 3 presents the results of the numerical experiments. The last section contains the summary and conclusions.

2 NUMERICAL MODEL

In this paper, we consider the solar atmosphere which consists of partially ionized hydrogen plasma which dynamics can be described by the set of non-ideal and non-adiabatic two-fluid equations with operating ionization and recombination for ions (protons) + electrons and neutrals (hydrogen atoms). These equations and the adopted numerical methods were described in detail by Murawski et al. (2022). Here, we use the extra heating term which is equal to 99 % of the thin radiation, and limit ourselves to a presentation of all the necessary information only that are utilized in the numerical setup.

Initially (at $t = 0$ s), we set the magnetohydrostatic equilibrium with hydrostatic ion and neutral gas pressures and mass density profiles (Murawski et al. 2022) which result from the semi-empirical temperature profile, $T_0(y)$, of (Avrett & Loeser 2008). See Fig. 1 for the temperature (top) and mass density (bottom) profiles. Note that ion mass density, ϱ_i, is about 100 times smaller than neutral mass density, ϱ_n, at $y = 0$ Mm. At $y \approx 1.3$ Mm $\varrho_\mathrm{i} = \varrho_\mathrm{n}$ and higher up in the chromosphere and in the solar corona, ϱ_i becomes larger than ϱ_n. The hydrostatic profiles are overlaid by the arcade magnetic field that is given as

$$\mathbf{B} = B_\mathrm{a}\left[\cos\left(\frac{x+L_\mathrm{B}}{\Lambda_B}\right), -\sin\left(\frac{x+L_\mathrm{B}}{\Lambda_B}\right), 0\right] e^{-y/\Lambda_B} + [0, B_\mathrm{v}, B_\mathrm{t}]\,. \quad (1)$$

Here, B_a, B_v and B_t correspond respectively to a magnetic carpet, modelled by the set of arcades, vertical and transversal components of magnetic field, $L_\mathrm{B} = 0.64$ Mm is the half-size of a single arcade, and $\Lambda_B = 2L_\mathrm{B}/\pi$ denotes a height over which B falls off $e-$times.

Figure 2 (top) illustrates spatial profiles of $T_\mathrm{i}(x, y, t = 0\,\mathrm{s})$ and magnetic field lines which correspond to Eq. (1) with $B_\mathrm{a} = 0.2$ G, and are set initially, at $t = 0$ s. It should be noted that the magnetic carpet is located below the transition region that is initially set at $y \approx 2.1$ Mm. As a result of the implementation of the vertical magnetic field, $B_\mathrm{v} = -5$ G, there are seventeen magnetic null points (Fig. 2, top). The transverse component of magnetic field is chosen as $B_\mathrm{t} = 1$ G. This choice of B_v and B_t is appropriate for the upper chromosphere and the corona.

To solve the two-fluid equations numerically, we use the JOANNA code (Wójcik et al. 2020). Along the y-direction we covered the numerical domain with 512 cells in the fine grid zone which occupies the region $(-3.0 \le y \le 17.48)$ Mm. Higher up, the grid is stretched and consists of 16 cells up to $y = 25$ Mm. The size of the numerical box along the $x-$direction is $(-20.48 \le x \le 20.48)$ Mm and it is covered by 1024 cells, leading to the finest grid resolution of $\Delta x = \Delta y = 40$ km. The plasma quantities are maintained at their equilibrium values at the top and bottom boundaries of the numerical box, while at the left- and right-sides periodic boundary conditions are implemented.

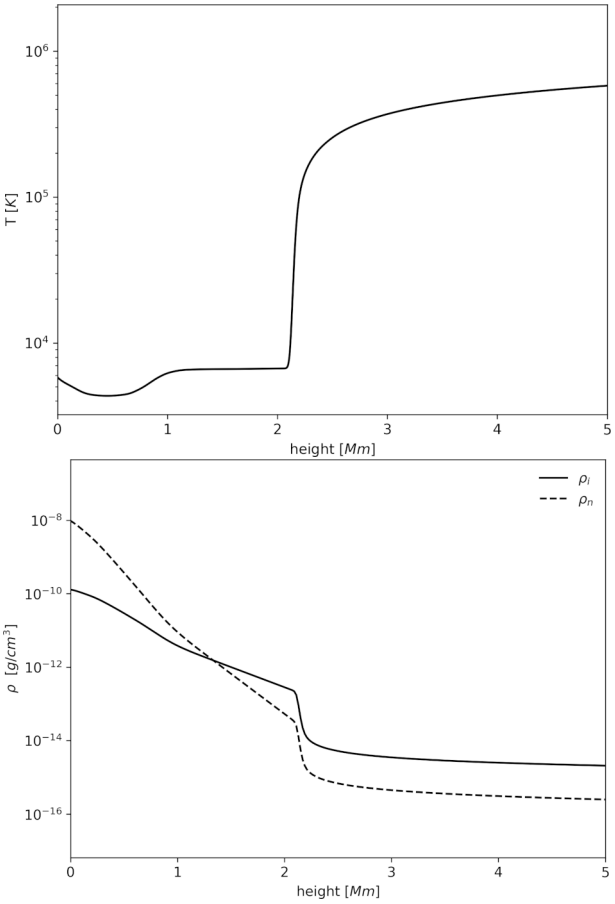

Figure 1. Variation with height, y, of the initial temperature, T_0, (top) and ion (solid line) and neutral (dashed line) mass densities (bottom).

3 NUMERICAL RESULTS

In this section, we present the dynamics of the model solar atmosphere in two regimes of the magnetic carpet, namely Ba = 0.2 G and Ba = 0.075 G.

3.1 The case of $B_\mathrm{a} = 0.2$G

We display results here for $B_\mathrm{a} = 0.2$ G. See Eq. (1). The waves are excited by the self-generated and self-evolving solar granulation which reshuffles magnetic field lines particularly strongly at the bottom of the photosphere and below it. The granulation mechanism takes place at the bottom of the photosphere, where convective instabilities lead to the formation of the turbulent flows there. These flows are associated with the perturbation of the initial state (Fig. 2, top) and thus the ejection of ions and neutrals to the higher layers of the atmosphere. The jets shown on the spatial profile of $\log(T_\mathrm{i})$ (Fig. 2, bottom) are generated by the solar granulation which leads to reconnection of magnetic field lines and thermal energy release in the photosphere and the chromosphere. This release in the chromosphere results in the largest jet which arrives to a height of about $y = 10$ Mm and it is located at $x = -6$ Mm.

In a progress of time the magnetic carpet evolves into complex magnetic arcades in the upper atmospheric layers. The jets obtained in the numerical experiments for $B_\mathrm{a} = 0.2$ G reach higher altitudes than in the initially straight magnetic field system which was considered by Murawski et al. (2022). At the foot-points of this carpet, that

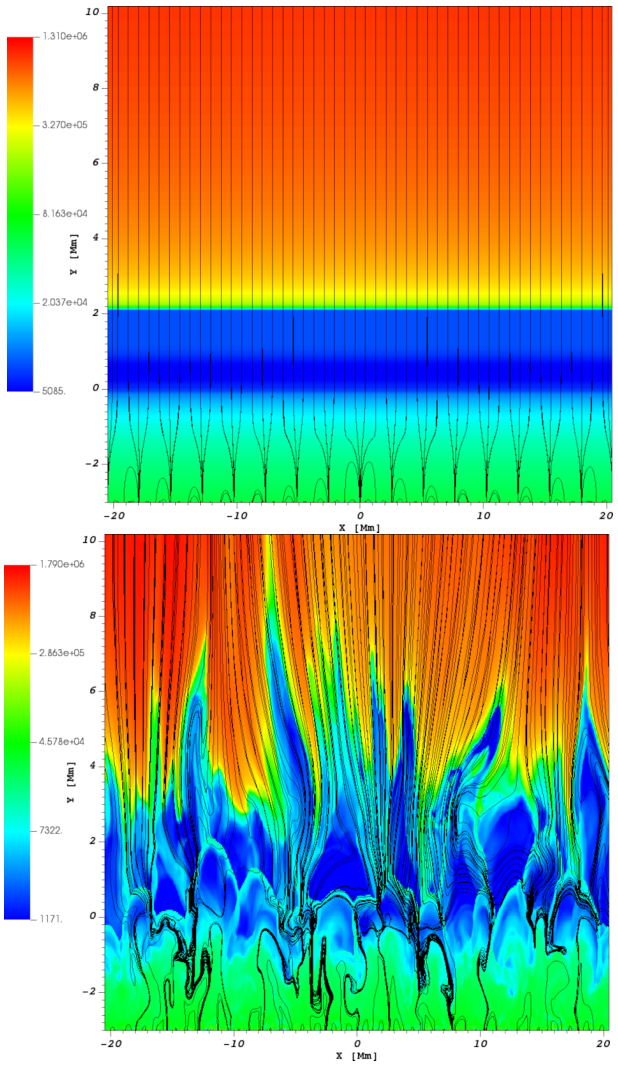

Figure 2. Spatial profiles of $\log(T_\mathrm{i})$ at $t = 0$ s (top) and $t = 5000$ s (bottom), overlaid by magnetic field lines which correspond to a magnetic carpet with $B_\mathrm{a} = 0.2$ G.

is below $y = 0$ Mm, magnetic field lines form the small magnetic flux-tubes of $B \approx 1332$ G and with strong downflows (Murawski et al. 2022).

In the presentation of the numerical results, we use below averaged plasma quantities:

$$\langle f \rangle_\mathrm{x} = \frac{1}{x_2 - x_1} \int_{x_1}^{x_2} f \, dx, \tag{2}$$

$$\langle f \rangle_\mathrm{xt} = \frac{1}{t_2 - t_1} \int_{t_1}^{t_2} \langle f \rangle_\mathrm{x} \, dt. \tag{3}$$

Here, $t_1 = 1000$ s, $t_2 = 5000$ s, $x_2 = -x_1 = 20.48$ Mm, and f is a plasma quantity such as a horizontally averaged vertical component of ion velocity, V_iy, and relative ion temperature perturbations,

$$\Delta T_\mathrm{i} = \frac{T_\mathrm{i} - T_0}{T_0}. \tag{4}$$

Plasma motions are in the form of upflows and downflows which are accompanied by two-fluid ion magnetoacoustic-gravity, neutral acoustic-gravity, and Alfvén waves. Maximum value of the averaged ion velocity, $\left\langle V_\mathrm{iy} \right\rangle_\mathrm{x}$, reaches about 44 km s^{-1} (Fig. 3, top-left). Note that $\left\langle V_\mathrm{iy} \right\rangle_\mathrm{xt}$ attains its minimum of about -6.5 km s^{-1} at $x = 1$ Mm. Higher up $\left\langle V_\mathrm{iy} \right\rangle_\mathrm{xt}$ grows with y and at $y \approx 10$ Mm it reaches its positive values, resulting in a net plasma outflows in the corona. See Fig. 3 (bottom-left).

The solar granulation results in ejection of ions and neutrals from the chromosphere, which while arriving to the transition region result in its oscillations. See Fig. 3 (top-right), illustrating time-distance plots for $\langle T_\mathrm{i} \rangle_\mathrm{x}$. Note that the transition region bounces up and down with oscillations which progressively calm down in time.

As a consequence of ion-neutral collisions, the excited waves are dissipated. This effect is most effective at the places, where the difference between the velocities of ions and neutrals is being the largest (Martínez-Sykora et al. 2020). See Fig. 4 which illustrates the vertical component of the ion-neutral velocity drift, $\left\langle V_\mathrm{iy} - V_{ny} \right\rangle_\mathrm{x}$. This drift attains its largest values in the transition region and low corona, which is in a good agreement with Murawski et al. (2022). It results from the weak coupling of ions and neutrals in the higher layer of the solar atmosphere and strong coupling in the lower regions. Thus they propagate with essentially the same speed in the photosphere and the chromosphere. Note that in the low corona during the initial phase $\left\langle V_\mathrm{iy} - V_{ny} \right\rangle_\mathrm{x} > 0$. Hence at $t < 1500$ s, as a result of the Lorentz force acting on them, ions attain higher velocities than neutrals which are not directly affected by this force.

The horizontally and time-averaged relative ion temperature, $\langle \Delta T_\mathrm{i} \rangle_\mathrm{xt}$, illustrates lower values compared to the semi-empirical data of Avrett & Loeser (2008) in the upper part of the convection zone and lower corona. Note that the horizontally and temporally averaged velocity reaches negative values, $\left\langle V_\mathrm{iy} \right\rangle_\mathrm{xt} < 0$, below the altitude $y = 6$ Mm. However, above this level, $\left\langle V_\mathrm{iy} \right\rangle_\mathrm{xt}$ attains positive values, which reveals the net plasma outflows. A comparison with Murawski et al. (2022) findings shows that the maximum $\left\langle V_\mathrm{iy} \right\rangle_\mathrm{x}$ values in both models are similar. But our results show a higher contribution of plasma outflows compared to plasma downflows with the opposite trend reported by Murawski et al. (2022). This is a significant new aspect as evident in the system of magnetic carpet with $B_\mathrm{a} = 0.2$ G. Besides, the simplified model of radiative losses, used in our model, may lead to the flows at the transition region and to its smoothing as it is evident in the averaged temperature profile in Fig. 2 (bottom-right panel).

In stratified medium such as the solar atmosphere, cutoff periods is an important quantity that determines the wave period ranges below which waves are able to propagate upwards (e.g. Routh et al. 2020). Figure 5 illustrates wave periods obtained from the Fourier spectra for $\left\langle V_\mathrm{iy} \right\rangle_\mathrm{x}$ (Fig. 3, top-left). We observe that at the heights within the range 0Mm < y < 1.5 Mm, the main wave period is about $P = 250$ s. For $y > 1.5$ Mm, the dominant wave period corresponds to $P \approx 340$ s. It is well known that waves with a period $P \approx 300$ s are evanescent in the photosphere (e.g. Wójcik et al. 2018) and therefore waves of these wave periods are unable to extend to higher altitudes. A comparison with Murawski et al. (2022) reveals that in both cases, we observe multiple wave power concentrations for various periods and heights. However, our results show weaker agreement with the observational data.

3.2 The case of $B_\mathrm{a} = 0.075$G

We present results here for $B_\mathrm{a} = 0.075$ G. Figure 6 displays spatial profiles of $\log(T_\mathrm{i})$ (color maps) and magnetic field lines at $t = 5000$ s for $B_\mathrm{a} = 0.075$ G. There is a clear difference in the size of the jets: those from the magnetic carpet with Ba = 0.075 G reach an altitude of $y = 5$ Mm, while jets from Ba = 0.075 G reach $y = 10$ Mm. Addi-

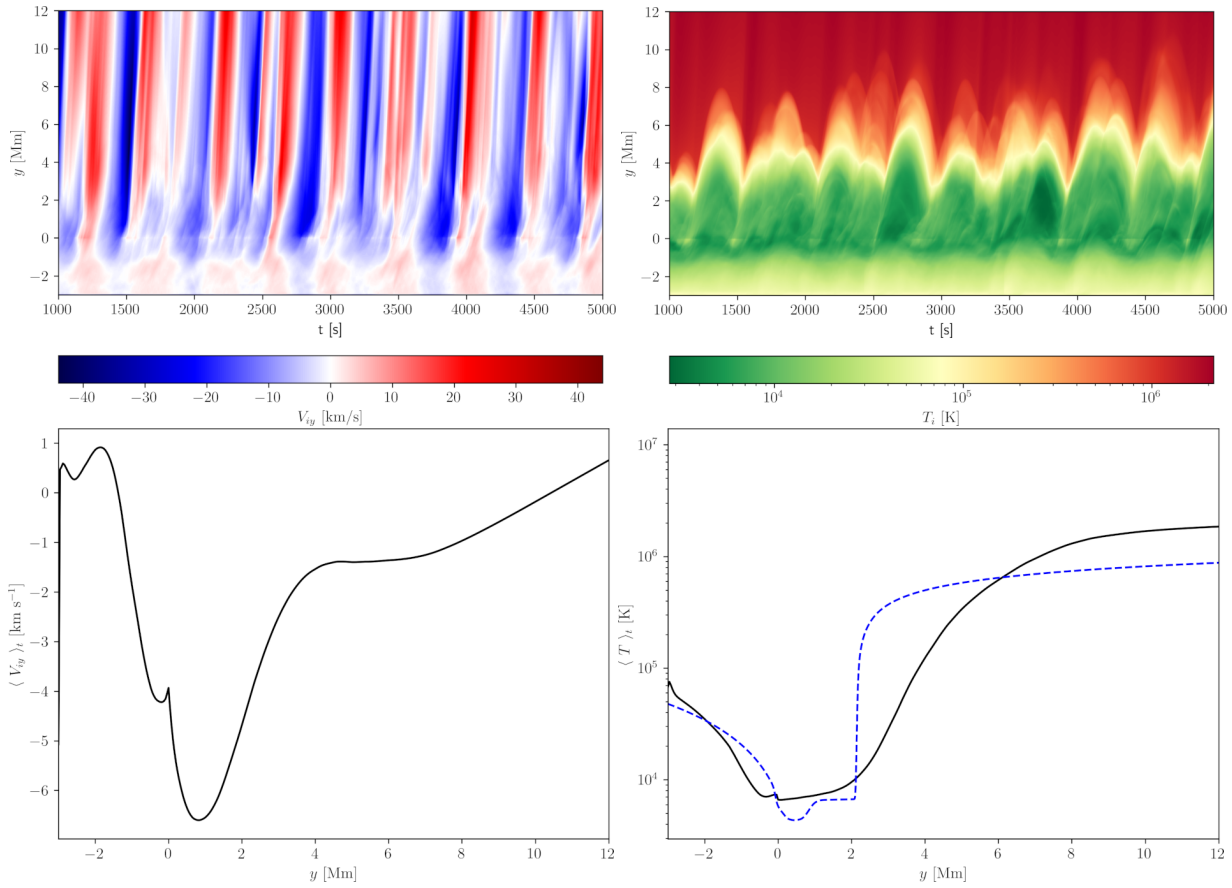

Figure 3. Time-distance (top) and averaged over time (bottom) plots for horizontally averaged $\langle V_{\rm iy} \rangle_{\rm x}$ (left) and $\langle T_{\rm i} \rangle_{\rm x}$ (right) (solid lines) for $B_{\rm a}$ = 0.2 G, $B_{\rm v}$ = −5 G and $B_{\rm t}$ = 1 G. Dashed line corresponds to Avrett & Loeser (2008) temperature profile (bottom right).

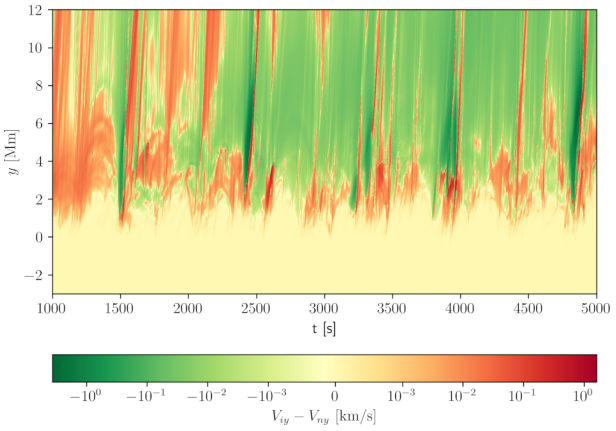

Figure 4. Time-distance plot for the horizontally averaged vertical component of ion-neutral velocity drift, $\left\langle V_{\rm iy} - V_{\rm ny} \right\rangle_{\rm x}$, in the case of $B_{\rm a}$ = 0.2 G.

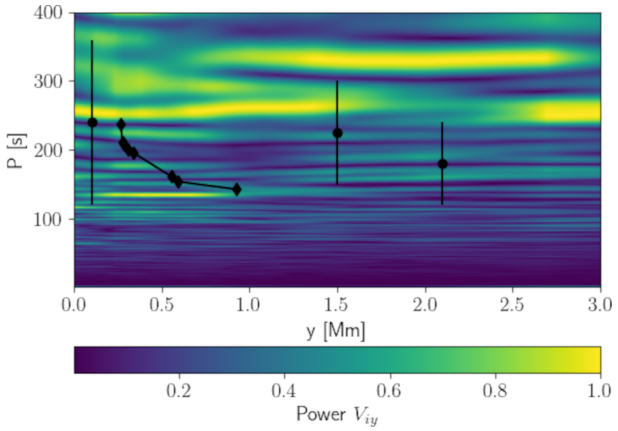

Figure 5. Fourier power spectrum of wave period P for $\langle V_{\rm iy} \rangle_{\rm x}$ vs. height for $B_{\rm a}$ = 0.2 Gs. The diamonds and dots correspond to the observational data obtained by respectively Wiśniewska et al. (2016) and Kayshap et al. (2018).

tionally, we observe that the higher $B_{\rm a}$ value affects higher maximum temperature of ions.

Figure 7 illustrates time-distance plots for vertical component of ion velocity, $\left\langle V_{\rm iy} \right\rangle_{\rm x}$, (top-left) and ion temperature, $\langle T_{\rm i} \rangle_{\rm x}$, (top-right), averaged over the horizontal direction. From the magnetic carpet studies, we infer that increasing $B_{\rm a}$ from $B_{\rm a}$ = 0.075 G to $B_{\rm a}$ = 0.2 G affects significantly max($\left\langle V_{iy} \right\rangle_{\rm x}$) which increases from about 19 km s^{-1} for the arcade magnetic field of Ba = 0.075 G to about 43 km s^{-1} for $B_{\rm a}$ = 0.2 G. Such increment of the ion vertical flows is anticipated as a stronger magnetic field corresponds to a much larger Lorentz force. Additionally, we observe change in the height that the oscillations of the transition region reach which is higher for $B_{\rm a}$ = 0.2 G. For the two $B_{\rm a}$ values studied in this article, we observe plasma outflows in the corona, while the photosphere and the chromosphere are dominated by the downflows. However, $\left\langle V_{iy} \right\rangle_{\rm xt} > 0$ are present in the corona for higher altitudes for the mag-

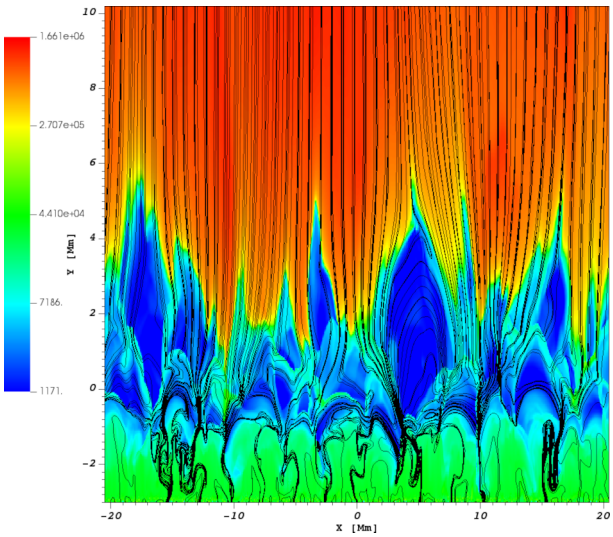

Figure 6. Spatial profiles of $\log(T_i)$ at $t = 5000$ s, overlaid by magnetic field lines which correspond to a magnetic carpet for $B_a = 0.075$ G.

netic carpet with $B_a = 0.2\ G$, viz. $y \approx 10$ Mm, than for the magnetic carpet with $B_a = 0.075\ G$, $y \approx 5.5$ Mm (Fig. 7, bottom-left).

Figure 8 presents wave period, P, vs. height, obtained from the Fourier power spectra for $\left\langle V_{iy} \right\rangle_x$ for $B_a = 0.075$ G. In this case, we can distinguish two dominant periods, namely $P \approx 320$ s (observed in for $B_a = 0.2$ G for $y > 0.7$ Mm) and $P \approx 270$ s, illustrated by the two yellow strips. The former period is surprisingly present essentially at every height; such long period waves are anticipated to be evanescent as periods higher than the cutoff period correspond to non-propagating waves (Kuźma et al. 2024). As a result, we infer that the plasma background is altered in time, increasing the cutoff period and allowing so large period waves to propagate from the photosphere through the chromosphere into the corona. The latter period is seen at $y \approx 0.5$ Mm and higher up, which evidences that such period waves propagate freely into the corona. Besides these two major wave periods, shorter periods waves with P being within the range of about $100 - 200$ s are also generated by the granulation and they are seen throughout the whole atmosphere. For $B_a = 0.2$ G $P \approx 250$ s does not show up for 1.5 Mm < y < 2.5 Mm. Comparison with the observational data of Wiśniewska et al. (2016) (diamonds) and Kayshap et al. (2018) (dots) reveals some level of agreement at certain altitudes.

4 SUMMARY AND CONCLUSIONS

We performed 2.5 D numerical experiments of the solar atmosphere that is modelled by two-fluid equations with non-adiabatic, non-ideal effects and ionization/recombination effects taken into account. We aimed to investigate chromosphere heating and generation of plasma outflows as well as Fourier power spectrum of the excited waves.

Our results can be summarized as follows. The developed numerical model showed that the self-generated and self-evolving solar granulation, along with the considered magnetic field configuration in the form of a magnetic carpet, facilitates the generation of all two-fluid waves, heating and flows. The study considered magnetic carpets with $B_a = 0.2$ G and $B_a = 0.075$ G. Given the observations (e.g. via the Hanle effect) which indicate a field strength of about 70 G in the mid-photosphere, these values are initially (at $t = 0$ s) small. However, the self-generated and self-evolved granulation alters the magnetic field which is organized in flux-tubes with mximum magnitudes of magnetic field of about $\mathbf{B} = 1332$ G and $\mathbf{B} = 650$ G for $B_a = 0.2$ G and $B_a = 0.075$ G, respectively. From the obtained numerical results, we infer that energy carried to the upper atmospheric layers thermalize and, as a result of the ion-neutral collisions, leading to localized heating of the chromosphere. Note that for both B_a, $\langle T_i \rangle_{xt}$ reaches higher values than the semi-empirical temperature model of Avrett & Loeser (2008) in the entire photosphere and chromosphere and the only distinguishable difference occurs in the corona. Nevertheless, the numerical findings of Murawski et al. (2022) show better agreement with semi-empirical temperature data of Avrett & Loeser (2008) than in our case (Fig 3, right-bottom). We speculate that it may be caused by the use of the different values of the extra heating implied in the corona, mainly, in our case the extra heating balanced 99 % of the thin cooling and 100 % in Murawski et al. (2022).

The resulting plasma heating is accompanied by plasma outflows. Hence, all the two cases, we consider here, can be the source of the nascent solar wind due to certain degree of plasma outflows generated in the corona. At higher altitudes, the magnetic carpet in the quiet-Sun effectively transport the plasma contributing to the origin of the nascent solar wind and mass cycle in the solar atmosphere. This result converges with the finding of Tu et al. (2005) and Tian et al. (2010) who suggest that the solar wind originates from coronal funnels above $y = 5$ Mm.

Studies of the magnetic carpets, specified by initially smaller and larger values of magnetic fields, B_a, show clear differences in the size of the generated jets and plasma oscillations. Additionally, we observe increase of the plasma velocity for higher B_a, which is anticipated as larger vertical ion flow may result from higher Lorentz force. The difference between the solutions corresponding to the different values of B_a is supposed to disappear after a long time. These solutions are anticipated to become statistically indistinguishable as time goes to infinity, and the differences present at any finite time represent transients of the initial condition.

The results obtained for the wave periods exhibit dominant periods and reveal some level of agreement with the observational data of Wiśniewska et al. (2016) and Kayshap et al. (2018) at some altitudes.

While the developed model mimics some aspects of the excited wave spectrum, the chromosphere heating and generation of plasma outflows, they do not show the whole scenario, and a more sophisticated treatment is required. Taking into account additional mechanisms to describe the solar atmosphere more accurately is a major challenge. Thus, such investigations are devoted to the future research.

ACKNOWLEDGEMENTS

KM's work was done within the framework of the project from the Polish Science Center (NCN) Grant No. 2020/37/B/ST9/00184. We gratefully acknowledge Poland's high-performance computing infrastructure PLGrid (HPC Centers: ACK Cyfronet AGH) for providing computer facilities and support within computational grant no. PLG/2022/015868. A part of numerical simulations was run on the LUNAR cluster at the Institute of Mathematics at M. Curie-Skłodowska University in Lublin, Poland. AKS acknowledges RAC-ISRO grant for the support of his scientific research. We visualize the simulation data using the ViSIt software package (Childs et al. 2012) and Python scripts.

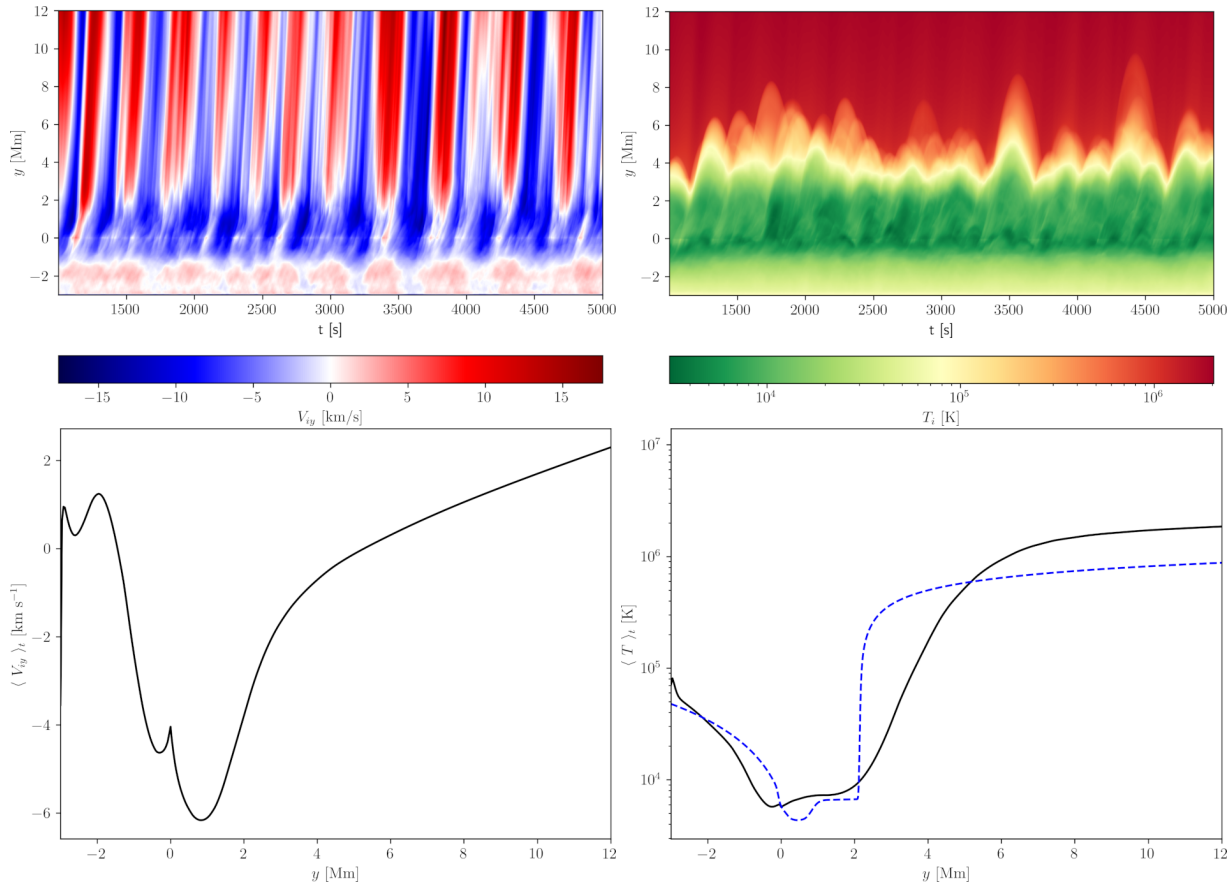

Figure 7. Time-distance (top) and averaged over time (bottom) plots for horizontally averaged $\langle V_{\rm iy} \rangle_{\rm x}$ (left) and $\langle T_{\rm i} \rangle_{\rm x}$ (right) for $B_{\rm a} = 0.075$ G.

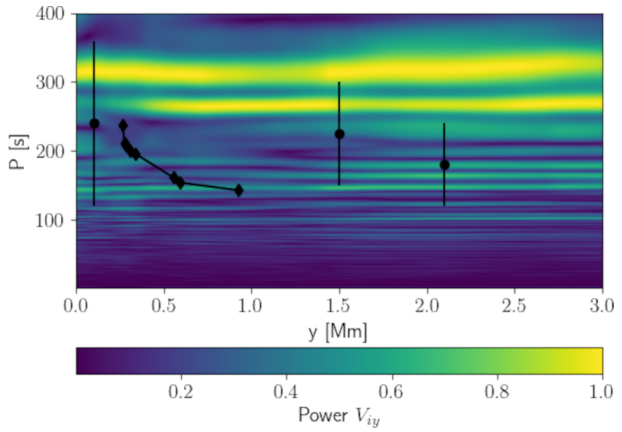

Figure 8. Fourier power spectrum of wave period P for $\left\langle V_{\rm iy} \right\rangle_{\rm x}$ vs. height for $B_{\rm a} = 0.075$ G. The diamonds and dots correspond to the observational data obtained by Wiśniewska et al. (2016) and Kayshap et al. (2018).

DATA AVAILABILITY

All data underlying the results are available in the article and no additional source data are required.

REFERENCES

Avrett E. H., Loeser R., 2008, ApJS, 175, 229
Ballester J. L., et al., 2018, Space Sci. Rev., 214, 58
Childs H., et al., 2012, VisIt: An End-User Tool For Visualizing and Analyzing Very Large Data. Chapman and Hall/CRC
Erdélyi R., James S. P., 2004, A&A, 427, 1055
Fleck B., Carlsson M., Khomenko E., Rempel M., Steiner O., Vigeesh G., 2021, Philosophical Transactions of the Royal Society of London Series A, 379, 20200170
Forteza P., Oliver R., Ballester J. L., Khodachenko M. L., 2007, A&A, 461, 731
Hansteen V. H., De Pontieu B., Rouppe van der Voort L., van Noort M., Carlsson M., 2006, ApJ, 647, L73
Heggland L., Hansteen V. H., De Pontieu B., Carlsson M., 2011, ApJ, 743, 142
Kayshap P., Murawski K., Srivastava A. K., Musielak Z. E., Dwivedi B. N., 2018, MNRAS, 479, 5512
Khomenko E., Collados M., Díaz A., Vitas N., 2014, Physics of Plasmas, 21, 092901
Kuźma B., Kadowaki L. H. S., Murawski K., Musielak Z. E., Poedts S., Yuan D., Feng X., 2024, Philosophical Transactions of the Royal Society of London Series A, 382, 20230218
Li K. J., Xu J. C., eng W. F., Xie J. L., Shi X. J., Deng L. H., 2024, arXiv e-prints, p. arXiv:2401.02617
Martínez-Sykora J., De Pontieu B., Hansteen V. H., Rouppe van der Voort L., Carlsson M., Pereira T. M. D., 2017, Science, 356, 1269
Martínez-Sykora J., Szydlarski M., Hansteen V. H., De Pontieu B., 2020, ApJ, 900, 101
Murawski K., Musielak Z. E., Poedts S., Srivastava A. K., Kadowaki L., 2022, Ap&SS, 367, 111
Niedziela R., Murawski K., Kadowaki L., Zaqarashvili T., Poedts S., 2022, A&A, 668, A32
Parnell C. E., 2002, MNRAS, 335, 389
Pelekhata M., Murawski K., Poedts S., 2023, A&A, 669, A47

Proctor M. R. E., 2004, Astronomy and Geophysics, 45, 4.14
Routh S., Musielak Z. E., Sundar M. N., Joshi S. S., Charan S., 2020, Ap&SS, 365, 139
Srivastava A. K., et al., 2021, Journal of Geophysical Research (Space Physics), 126, e029097
Tian H., Tu C., Marsch E., He J., Kamio S., 2010, ApJ, 709, L88
Tu C.-Y., Zhou C., Marsch E., Xia L.-D., Zhao L., Wang J.-X., Wilhelm K., 2005, Science, 308, 519
Vigeesh G., Jackiewicz J., Steiner O., 2017, ApJ, 835, 148
Wiśniewska A., Musielak Z. E., Staiger J., Roth M., 2016, ApJ, 819, L23
Wójcik D., Murawski K., Musielak Z. E., 2018, MNRAS, 481, 262
Wójcik D., Kuźma B., Murawski K., Musielak Z. E., 2020, A&A, 635, A28
Zaqarashvili T. V., Khodachenko M. L., Rucker H. O., 2011, A&A, 529, A82
del Pino Alemán T., Trujillo Bueno J., Štěpán J., Shchukina N., 2018, ApJ, 863, 164